Materials Horizons

COMMUNICATION

View Article Online
View Journal | View Issue

Cite this: *Mater. Horiz.*, 2017, 4, 477

Received 20th February 2017,
Accepted 27th March 2017

DOI: 10.1039/c7mh00104e

rsc.li/materials-horizons

A highly sensitive graphene woven fabric strain sensor for wearable wireless musical instruments†

Xu Liu,[a] Chen Tang,[a] Xiaohan Du,[a] Shuai Xiong,[a] Siyuan Xi,[a] Yuefeng Liu,[a] Xi Shen,[a] Qingbin Zheng,*[ab] Zhenyu Wang,[a] Ying Wu,[a] Andrew Horner[c] and Jang-Kyo Kim *[a]

Highly flexible and sensitive strain sensors are essential components of wearable electronic devices. Herein, we present a novel graphene woven fabric (GWF)/polydimethylsiloxane (PDMS) composite as a highly flexible, sensitive strain sensor capable of detecting feeble human motions with an extremely high piezoresistive gauge factor of 223 at a strain of 3% and excellent durability. A wireless wearable musical instrument prototype made of the composite sensor demonstrates conversion of human motions to music of different instruments and sounds.

Conceptual insights

Highly sensitive, flexible GWF/PDMS composite sensors are integrated with Bluetooth wireless communication and a smartphone to create a wireless wearable musical instrument. The first of its kind, a graphene-based flexible composite is prepared as a skin-mountable device to convert human body motions to controllable music by bridging the technological gap between signal collection, processing and transmission in wearable strain sensors. The composite possesses excellent electrical conductivity arising from the CVD-grown graphene, good stretchability and durability due to the flexible polymer matrix. The change in electrical resistance is sensitive to small strains in both tensile and bending loads, as well as the loading direction due to the orthotropic organization of graphene tubes in the woven fabric structure. Therefore, the sensors deliver a high sensing capability response to tiny deformations with an exceptionally high gauge factor at a low strain in real wearable applications. Herein, we demonstrate a prototype of a musical instrument on a smartphone, which is capable of transmitting finger and muscle motions to voltage changes in circuits and converting them into sounds and music from a smartphone through Bluetooth wireless technology. This work not only offers insights into diverse applications of highly sensitive graphene-based composite sensors, but also opens new potential of graphene composites to fabricate multifunctional devices for emerging areas, like healthcare and mobile electronics.

Transparent and flexible sensing devices are becoming increasingly important to satisfy functional and structural demands for wearable and skin-mountable devices.[1–5] Wearable sensors must meet several critical requirements, including lightweight for easy carrying, a high sensitivity for monitoring tiny human motions, high flexibility and stretchability to accommodate large deformations, high durability with low failure risks, and biocompatibility for skin-mountable applications. The existing commercially available sensors made of metals and semiconductors are relatively cheap, but the limited flexibility and sensitivity have significantly hindered their potential in wearable applications. Various nanomaterials, including metal nanowires,[6–8] metal thin films,[9] nanoparticles,[10] silicon nanoribbons,[11] carbon blacks,[12] carbon nanotubes,[13–16] or graphene[3,17–23] coupled with elastomeric substrates, have been explored as stretchable and sensitive devices. However, metal-based nanowires, nanoribbons and nanoparticles have some critical limitations, such as complex fabrication procedures with high materials and manufacturing costs, low sensitivity in the small strain range and poor reversibility, which must be addressed to meet various requirements. For example, pre-strained silver nanowire (AgNW) sensors possess reasonable sensitivity to applied strains based on the percolated conductive networks,[24] where the tunnelling effect and disconnection between AgNWs allow large strains to be detected. However, the fabrication of conductive AgNW networks involves a series of chemical reactions and assembly procedures. Another example is the ZnO/polystyrene (PS) nanowire hybrid film[25] that showed high tolerable strains at the expense of high costs due to the relatively complex fabrication process. Nanoparticle-based sensors not only need complex synthesis processes, but also require patterning of the nanoparticles to realize sensing capability.[26,27]

Low-dimensional carbon materials, especially carbon nanotubes (CNTs) and graphene, in the form of films,[13,28,29] fibers,[15,22] composites,[3,20,30,31] foams,[32] ripples/wrinkles,[18,33,34] and meshes,[35–37] have drawn great attention due to their

[a] Department of Mechanical and Aerospace Engineering, The Hong Kong University of Science and Technology, Clear Water Bay, Kowloon, Hong Kong. E-mail: mejkkim@ust.hk; Fax: +852 2358 1543
[b] Institute for Advanced Study, The Hong Kong University of Science and Technology, Clear Water Bay, Hong Kong. E-mail: mezheng@ust.hk
[c] Department of Computer Science and Engineering, The Hong Kong University of Science and Technology, Clear Water Bay, Hong Kong

† Electronic supplementary information (ESI) available. See DOI: 10.1039/c7mh00104e

excellent flexibility, conductivity and transparency compared with other materials, such as metals, metal oxides and silicon particles. Although the stretchability of CNT-based strain sensors can be extremely high, their gauge factors (GFs), which are defined as the ratio of normalized change in electrical resistance ($\Delta R/R_0$) to the mechanical strain ε, are relatively low ranging from 3–62[13,31,33] due to their one-dimensional structure. Taking advantage of high electrical conductivities, excellent optical transparency, easy patterning and an ultra-high sensitivity,[1,38] graphene-based structures are excellent candidates for piezoresistive strain sensors. However, the sensitivities of pristine graphene films are low under a moderate strain because there is no band gap opening effect;[39] while the hexagonal atomic structure of graphene may be partially destroyed when a high tensile strain is applied, leading to the change in the electronic band structure and electrical resistance.[40,41] For example, the strain sensors made from chemical vapor deposition (CVD)-grown graphene had GFs of ~14 at a maximum strain of ~7%.[42,43] Graphene foams are highly flexible and amenable to compression and bending because of their three dimensional (3D) interconnected cellular morphology in both the in-plane and though-thickness directions. However, their relatively low GFs greatly hinder sensory applications requiring high sensitivities.[32,44–47]

One-step CVD-grown graphene woven fabrics (GWFs) have been considered an attractive option for piezoresistive strain sensors owing to both their outstanding mechanical flexibility and electrical conductivities.[48] GWFs possess a well-defined planar interwoven structure, making them highly responsive and sensitive to reversible deformations in the in-plane direction. Substantial reductions in thickness and weight compared to graphene foams make GWFs a potential conductive component for strain sensors with a high sensitivity and comfort particularly in skin-mountable applications. Although the sensing properties of GWF/PDMS composites have been investigated in different deformation modes, like tension, torsion and bending,[49,50] as well as after touching,[51] the sensing mechanisms of the given sensors need to be fully understood for their proper implementation and a prototype device is required to demonstrate real-world applications. For example, the effects of graphene growth condition and loading direction on sensing capability are not well understood. Further, developing a technique to fully integrate the sensors with other peripheral components into a more or less complete wearable platform that can find a wide range of monitoring applications is still a considerable challenge.

Herein, we present novel strain sensors made from GWF/PDMS composites with freestanding GWFs consisting of orthogonally interconnected graphene tube (GT) networks. We specifically studied the sensory capabilities of GWFs grown under different conditions and the sensing mechanisms of GWFs in a small range of strains. We identified the effect of GT orientation on sensitivity and resistance change of composite sensors, and formulated the corresponding theoretical models to establish the relationship between the sensory capabilities of GWFs in two different orientations and under tensile/bending strains. Further, we demonstrated a novel prototype of a wearable musical instrument by connecting the body motion sensors with wireless telecommunication tools and smartphone apps. Owing to the stable conductive networks, the GWF/PDMS composites were able to convert tiny mechanical deformations into noticeable electrical signals with an ultra-high sensitivity. To realize a fully integrated sensing system to extract information from body motions, we demonstrated a wearable musical instrument with fully programmable and configurable wireless sensor networks, allowing the users to manipulate music through small body motions.

Ni woven fabrics were used as templates for the synthesis of freestanding GWFs by a template-based CVD method, similar to our previous studies.[52–54] The Ni woven fabrics (with 200 meshes in a 25.4 × 25.4 mm^2 square and Ni wires of 56 μm in diameter, supplied by Beijing Century Woven Corp) were cleaned with diluted HCl, acetone and deionized (DI) water followed by ultrasonication. After drying in an oven for 24 h, the Ni substrates were cut into 100 mm × 50 mm rectangular pieces, which were placed in the quartz tube of a CVD furnace (Hefei Kejing Materials). The furnace was heated to 1000 °C at a rate of 17 °C min^{-1} and the Ni mesh was annealed under an Ar flow at 200 standard cubic centimeters per minute (sccm) and a H_2 flow at 100 sccm for 30 min. CH_4 with a concentration of 3.0 or 10.0 vol% in Ar and H_2 atmosphere was subsequently introduced into the furnace for 20 min. The furnace was rapidly cooled to ambient temperature under Ar and H_2 flows, allowing supersaturated carbon atoms to precipitate and form graphene layers on the Ni template surface. After etching the Ni skeleton by immersion in a 0.5 M $FeCl_3$/1 M HCl mixture solution at 80 °C for 2 h, freestanding GWFs were collected using a glass fiber cloth.

The fabrication processes of GWF/PDMS composites are schematically shown in Fig. 1a. PDMS solution (Sylgard184,

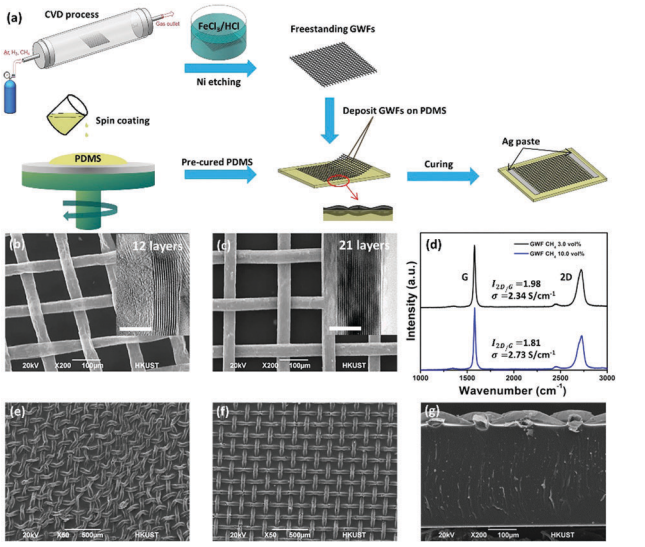

Fig. 1 (a) Schematic flowchart of the fabrication processes of GWF/PDMS composites. SEM images of freestanding GWFs grown using (b) 3.0 and (c) 10.0 vol% CH_4, insets are the TEM images and scale bars are 5 nm. (d) Raman spectra of freestanding GWFs. SEM images of GWF/PDMS composites containing different GWFs prepared using (e) 3.0 and (f and g) 10.0 vol% CH_4.

Dow Corning, base/curing agent = 10/1 by weight) was stirred for 1 h at room temperature, followed by degassing in a vacuum oven for 30 min. A PDMS thin film was produced by spin coating the PDMS solution on a polyethylene terephthalate (PET) film at 200 rpm for 1 min. Pre-cured sticky PDMS thin films with a thickness of ~400 μm were obtained after curing at 60 °C for 30 min in an oven. A freestanding GWF layer with a 25 mm × 5 mm rectangular shape was placed onto the pre-cured PDMS thin film at an angle of 0° (90°) or 45° (−45°) *vs.* the loading axis. After full curing at 80 °C for 2 h, the GWF/PDMS composites were peeled off from the PET substrate. The conductive silver paste was applied at both ends of GWFs to connect copper wires for interconnection.

An optical microscope (Olympus BX51M), a scanning electron microscope (SEM, JEOL-6390), and a transmission electron microscope (TEM, JEOL 2010) were used to characterize the morphologies of freestanding GWFs and composites. The Raman spectra of GWFs were obtained on a Micro-Raman spectrometer (Renishaw Micro-Raman/Photoluminescence System) using an Ar ion laser (514.5 nm emission). The tensile and three-point bending tests were carried out on a universal testing machine (MTS Alliane RT-5) at a cross-head speed of 1 mm min^{-1}. The resistances of the composites under loads were monitored by a data logger (34970A Data Acquisition/Data Logger Switch Unit, Agilent) at 1 Hz. A digital oscilloscope (Tektronix, TBS 1072B-EDU) was used to monitor the resistance change of GWF/PDMS composites when attached to different parts of the human body. The software ImageJ was employed to analyze the deformation of GTs using the optical images of GWF/PDMS composites.

After etching out the Ni skeleton, the freestanding GWFs consisted of interconnected hollow GTs, as shown in Fig. 1b and c, which looked essentially the same as the Ni mesh configuration. The GWFs prepared using a higher CH_4 concentration of 10.0 vol% (Fig. 1c) presented a firmer tube structure than those with a lower CH_4 concentration of 3.0 vol% (Fig. 1b) showing flattened GTs. The average numbers of graphene layers in the two GWFs were 21 and 12, respectively, as shown by the inset TEM images in Fig. 1c and b. The Raman spectra of GWFs given in Fig. 1d exhibit two prominent Raman peaks, namely G- and 2D-band peaks, at ~1580 and ~2700 cm^{-1}, respectively. The D-band peak at ~1350 cm^{-1} was almost negligible, demonstrating that the CVD-grown GWFs possessed high quality graphene with negligible defects. The intensity ratios, $I_{2D/G}$, were 1.98 and 1.81 for the GWFs grown with 3.0 and 10.0 vol% CH_4, respectively, as a result of the difference in the GT thickness. The thick GTs were essential for ensuring the integration of GWFs when transferring to the PDMS substrates (Fig. 1e and f) and the structural durability of the GWF/PDMS composites under repeated loading/unloading cycles. Similarly, the electrical conductivities, 2.34 and 2.73 S cm^{-1}, were much higher for the thicker GWFs than the thinner ones. Excellent adhesion between the GWF and PDMS matrix was realized by directly depositing the freestanding GWF on the sticky surface of the partially cured PDMS thin film. The strong adhesion between the GWF and PDMS substrate is particularly important for the strain sensing capability of the composite. After PDMS was fully cured, the GWF was partly embedded in the PDMS substrate (Fig. 1g).

To investigate the strain sensing properties of GWF/PDMS composites, the normalized resistance change ($\Delta R/R_0$) was traced at different loading conditions, where ΔR is the resistance change and R_0 is the initial resistance. The results from the uniaxial tensile tests accompanied by simultaneous resistance measurements (Fig. 2a) present an almost linear ($\Delta R/R_0$) *vs.* strain relationship with nearly or more than 200% changeat 3% strain for all GWF/PDMS composite samples studied, demonstrating them as highly sensitive strain sensors. It is also worth noting that their piezoresistive sensitivities depended on both the quality of GWFs and the orientation of GTs to the tensile axis. For example, the GWFs with different graphene thicknesses, which were grown using different CH_4 gas concentrations, showed different $\Delta R/R_0$ values for a given strain. The GWF/PDMS composites containing thicker GTs displayed a much higher sensitivity than those with thinner GTs. The GWFs with thicker GTs (Fig. 1f) maintained a stable and regular mesh configuration once transferred onto the PDMS, allowing an effective load transfer from PDMS to GWF under load. However, the GWFs with thinner GTs tended to shrink by deforming to a wavy structure during transfer (Fig. 1e). The latter composites showed almost no change in resistance in the initial 0.8% strain (Fig. 2a) because the highly irregular, wrinkled GTs had to recover their original configuration (Fig. S1a, ESI†). Delay may exist in the response due to the viscoelastic nature of PDMS.[1,6] A typical response time of ~0.072 s was measured for the GWF/PDMS composite sensors at a tensile strain of 3% and a loading speed of 1 mm min^{-1}, as shown in Fig. S6 (ESI†), indicating good adhesion between the GWFs and the PDMS matrix. Linearity is an important parameter for stretchable strain sensors because nonlinearity makes the calibration process complex and difficult.[1] The composites containing thicker GTs showed a higher R^2 value of 0.9884 for 0° (and 0.9871 for 45°) than the corresponding R^2 of 0.9412 for the thinner GTs, demonstrating that the stable GWF structure gave rise to higher linearity. In view of the stable and robust structure with a good linear response to tension, the GWF/PDMS composites containing thick GTs are considered suitable for strain sensing applications.

Besides the quality of GWFs, the orientation of GTs against the loading direction significantly affected the sensitivity of GWF/PDMS composites under uniaxial tension. It is found that the samples loaded in the same direction as the orthogonally-interconnected GTs, *i.e.* at 0°, presented an over threefold higher normalized resistance change than that loaded at an angle of 45° (Fig. 2a). To understand such differences, equivalent and simplified circuit models of GWF/PDMS composites were built to analyze the resistance change of composites (Fig. S4, ESI†). The GTs were considered as the interconnected resistors and the GTs in each unit had an inherent resistance, r_0. The GTs contained polycrystalline graphene sheets connected by a number of grain boundaries or wrinkles, reflecting the underlying polycrystalline Ni templates, and the interfacial resistance between the neighbouring graphene grains increased in tension due to the widening of the grain boundaries (Fig. 2b).[55] It is shown that these grain boundaries or wrinkles severely weakened the mechanical strength and modulus of graphene sheets/membranes[56,57]

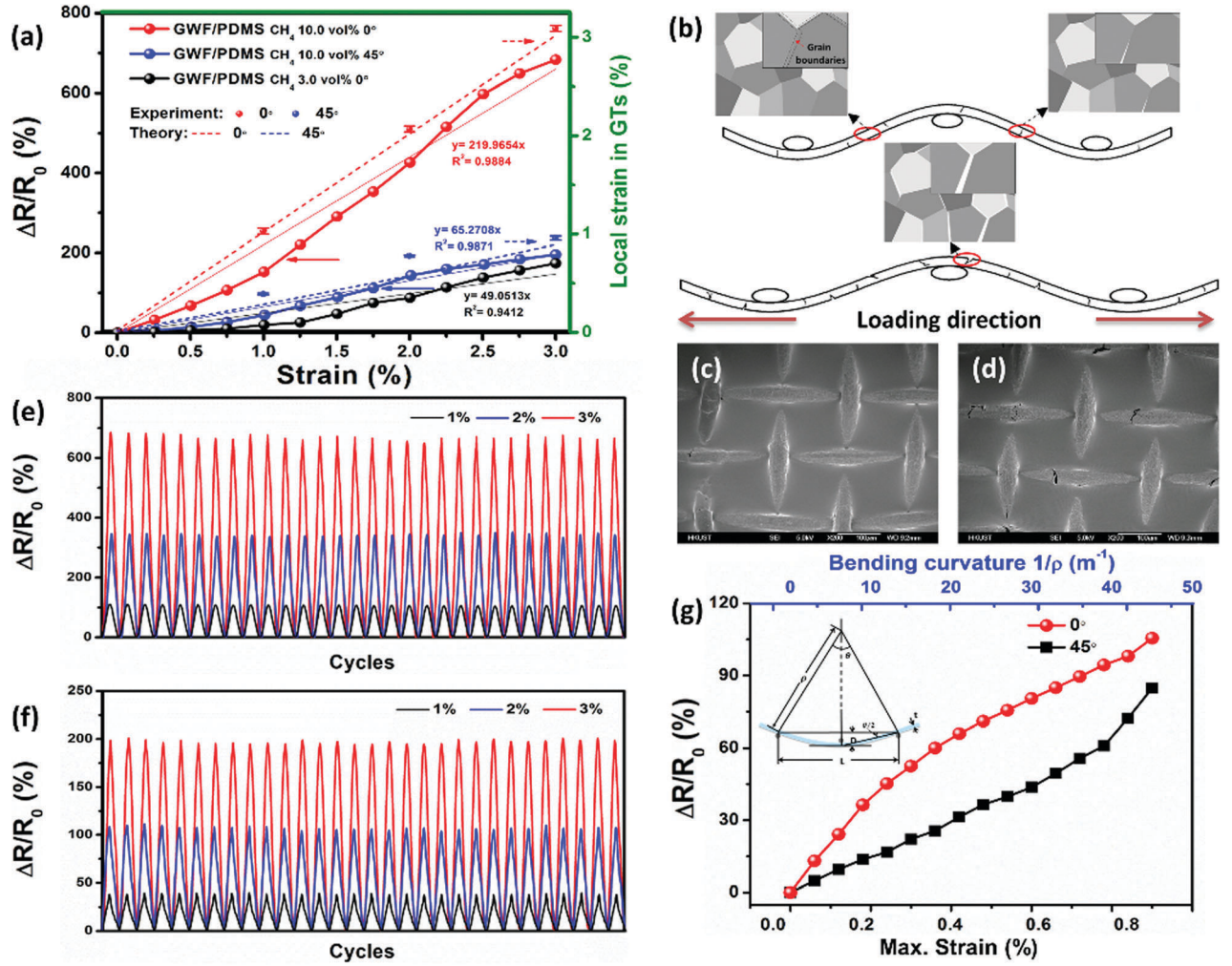

Fig. 2 (a) Normalized resistance change, $\Delta R/R_0$, of GWF/PDMS composites (three solid lines) and local strains in GTs (dash lines and filled circles) as a function of applied tensile strain. (b) Schematic of the formation of cracks along the grain boundaries of GTs after stretching. Cracks are formed after stretching on the graphene tube surface, especially along the grain boundaries. SEM images of the GWF/PDMS composite surface (c) before and (d) after stretching. Normalized resistance changes *vs.* cycles of GWF/PDMS composites with (e) GTs (0°) and (f) GTs (45°) as a function of applied strain in the cyclic tensile test. (g) Normalized resistance change of GWF/PDMS composites in three-point bending for different GT orientations as a function of maximum flexural strain and bending curvature, $1/\rho$. The inset shows a schematic of the three-point bending test and the relationship between bending curvature, bending angle and maximum strain.

although there was no apparent consensus on whether they impeded electrical transport, thus reducing the electrical conductivity of polycrystalline graphene.[58,59] With increasing strain in GTs, however, the graphene grains would eventually separate, forming many microcracks along the grain boundaries of GTs (Fig. 2b and d), which gradually disconnected the conductive pathways and increased the resistance of GTs. To quantify the above relationship, the normalized resistance change in GTs was assumed to be linearly proportional to the local strain:[36,60]

$$\Delta r/r_0 = k\cdot\varepsilon_l \quad (1)$$

where k is a constant and ε_l is the local strain in GTs. The contact resistances at the joint points were neglected in these simplified models. When tension was applied to the GWF/PDMS composites in the direction (0°) and at an angle of 45° to the GTs, the local strains in the GTs were denoted as ε_{0° and ε_{45°, respectively. The relationships between the applied strain to composites, ε, and the local strains in GTs were obtained using the strain transformation equation (see the ESI† for details):

$$\varepsilon_{0^\circ} = \varepsilon, \quad (2)$$

$$\varepsilon_{45^\circ} = \left(\frac{1-v}{2} + \frac{1+v}{2}\cos 2\theta'\right)\varepsilon, \quad (3)$$

where v is the Poisson's ratio of the composites and θ' is the angle between the GTs and the applied load after deformation. The angle θ' was determined by taking into account the shape change of the orthogonal GT network due to the Poisson's effect (see the ESI† for details):

$$\theta' = \arctan\frac{1-v\varepsilon}{1+\varepsilon}. \quad (4)$$

Based on the equivalent circuit models, the relationship between the normalized resistance changes in the composites,

$\Delta R/R_0$, and the local strains in the GTs when the tension was applied at two directions can be expressed by (see the ESI† for details):

$$\frac{\Delta R_{0^\circ}}{R_{0\,0^\circ}} = k \cdot \varepsilon_{0^\circ}, \quad (5)$$

$$\frac{\Delta R_{45^\circ}}{R_{0\,45^\circ}} = k \cdot \varepsilon_{45^\circ}. \quad (6)$$

The local strains in 0° GTs (ε_{0°) and 45° GTs (ε_{45°) given in eqn (2) and (3) are plotted as a function of applied strain (ε), as shown in Fig. 2a. To verify the predictions, the local strains in the GTs were determined by measuring the changes in length of GTs from the optical images taken at different tensile strains (Fig. S3, ESI†) under a microscope, as shown in Table S1 (ESI†). Both the predicted and measured values of ε_{0° were almost identical to the applied strain, ε, in the composite, whereas the corresponding values of ε_{45° were less than 30% of the applied strain, ε. The difference between the prediction and measurements of ε_{0° was less than ±5%, proving efficient transfer of the strain applied to the composites to GTs owing to the good adhesion between the GTs and PDMS matrix. The prediction of ε_{45° also agreed reasonably well with the measurements, indicating a simplified resistance model (Fig. S4 and ESI†) and that the assumptions given in eqn (1) were appropriate. In summary, the tension applied to the GWF/PDMS composites resulted in different local strain responses by the GTs depending on the angle between the directions of GTs and tensile loading. The difference in local strain response led to different sensitivities of the composites in terms of normalized resistance change, $\Delta R/R_0$: the composites loaded at 0° to the GT direction exhibited at least threefold higher $\Delta R/R_0$ than those loaded at 45° to the GT direction for the range of applied strains studied.

To confirm their durability and stability for practical sensing applications, the GWF/PDMS composites were subjected to cyclic tensile tests of repeated stretching and relaxing under different maximum applied strains of 1, 2 and 3%. The corresponding reversible resistance changes in the normalized form monitored during the cyclic tests are shown in Fig. 2e and f. The stress–strain curves presented high linearity and repeatability with very little hysteresis (see also Fig. S5 (ESI†) for the detailed stress–strain curves at different maximum strain levels), showing that the composites were in the linear elastic regimes under small strains (<3%). There was an almost perfectly linear relationship between the normalized resistance change and the applied strain during cyclic tests, demonstrating that the GWF/PDMS composites possessed an excellent linear and repeatable response to tiny strains. The durability of the GWF/PDMS sensors for long-term service was confirmed by cyclic tensile tests for 1000 cycles (Fig. S7, ESI†) where the $\Delta R/R_0$ responses remained almost uniform, confirming their excellent durability and repeatability for practical sensory applications.

Apart from the high sensitivity to uniaxial tensions, the GWF/PDMS composites also showed high sensitivity to bending, which is indeed a more common loading condition than uniaxial tension in human motions. To realize the detection of bending, the GWF/PDMS composite was attached onto a 100 μm PET slab, which was subjected to a three-point flexure. Fig. 2g plots the relative resistance changes of the GWF/PDMS composites in bending as a function of maximum strain at the mid-span and bending curvature (see the inset diagram, the ESI† and Fig. S8 for details of the relationship between the bending curvature, $1/\rho$, bending angle, θ, and the maximum flexural strain, ε_{max}, at the mid-span). The maximum flexural strain felt by the outer surface of the composite mid-span was 0.88% when the bending curvature was 44 m^{-1} (or an equivalent bending angle of 52.06°); while the flexural strains in the other parts away from the mid-span were increasingly smaller. Therefore, the normalized resistance changes of the composites in bending depend on the non-uniform strains in GTs, which were different from the uniform strain in GTs in uniaxial tension, as shown in Fig. 2a. Unlike the results shown in uniaxial tension, the resistance change was non-linear in bending. Similar to tension, however, the GWF/PDMS composites with 0° GTs showed a much higher sensitivity than those with 45° GTs. The resistance changes of GWF/PDMS composites arose mainly from two parts, *i.e.* the local strain in the GTs and the change in GT shape. In uniaxial tension, the strain is assumed to distribute uniformly along the whole length of the sample, leading to a uniform resistance change along the whole sample. In three-point bending (Fig. S8, ESI†), however, only the central part of the sample sustains a maximum local tensile stress/strain where the resistance change is also the maximum, thus leading to a much smaller average resistance change along the sample.

Fig. 3 presents a comparison of sensing capabilities between the current and existing graphene-based sensors. The sensitivity depended on many factors, including the intrinsic properties, the preparation method and the structure of graphene. Graphene

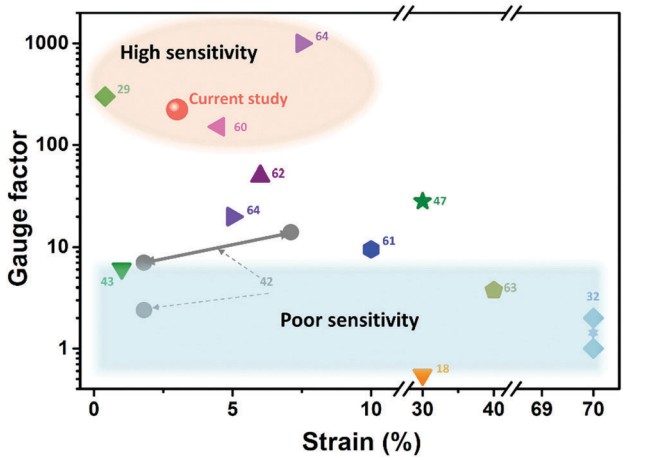

Fig. 3 Comparison of sensing capabilities between the current and reported graphene-based sensors. Experimental data: current study: ●; CVD-grown graphene: ◆ nanographene film,[29] ◆ fragmentized graphene foam,[32] ● Rosette type graphene,[42] ▼ wafer scale graphene,[43] ▲ graphene@PVA fiber,[62] ◀ monolayer graphene,[60] ⬟ monolayer graphene;[63] chemical derived graphene: ★ reduced graphene oxide foam,[47] ⬢ graphene stack-layers,[61] ▶ graphene ribbons;[64] mechanically cleaved graphene: ▼ graphene ripples.[18]

has an inherently low sensitivity because of its weak electrical response to mechanical deformation, requiring structural modifications to boost the piezoresistive sensitivity.[39,40] Many different methods, such as special patterning, CVD and rational assembly into 1D, 3D and aligned structures, have been applied with varied success. For example, pre-stretching the substrate introduced periodical graphene ripples, showing a GF ~0.55 at an applied strain up to 30%.[18] The graphene thin film sensors grown by a CVD method sustained only 1% strain with a GF of 6.1,[43] whereas the Rosette type graphene strain sensors possessed a GF of 2.4 at 1.8% strain and 4 to 14 at 1.8–7.1% strain.[42] The wafer-scale flexible strain sensors consisting of graphene micro-ribbons fabricated from one-step laser scribing had a GF of up to 9.49 at 10.0% strain.[61] Graphene/poly(vinyl alcohol) core/sheath fibers presented a GF of ~50 at ~6.3% strain.[62] The graphene sheets patterned by optical lithography and O_2 plasma etching showed a high GF of 151 at 4.5% strain.[60] A remarkable GF of about 300 was reported for graphene/mica composites at a strain lower than 0.4%[29] which is attributed to the large piezoresistive effect based on the charge tunnelling between adjacent nanographene islands. For 3D graphene structures, the controllable graphene/PDMS composites showed a low GF of 3.75 when loaded to 40% strain.[63] The reduced graphene oxide/polyurethane foam exhibited a GF of ~28.3 at 30% compressive strain;[47] while the fragmented graphene foam exhibited a GF of 15–29 at 70% strain.[32] The graphene ribbons consisting of mesh fabrics prepared by spinning graphene oxide hydrogel[64] presented a GF of ~20 at strains less than 5% and reached an exceptional GF of ~1000 at strains above 7.5% by employing a large amount of fracture points in the graphene structure. The present GWF/PDMS composites exhibited a GF of ~223 at 3% strain, showing a relatively high GF and sensing range due to the interconnected conductive graphene mesh structure.

Given the high sensitivity, good linearity, low hysteresis, excellent reproducibility and unique anisotropy of sensory capability of the GWF/PDMS composites, it is very appealing to use them as highly sensitive motion sensors for emerging wearable applications. Here, we demonstrate the practical application of GWF/PDMS composite sensors for a fully integrated, wireless, and wearable musical instrument (Fig. 4a). The idea is a conceptually new approach where the prototype musical instrument is built by consolidating graphene/polymer composite sensors into an open source hardware with wireless communication capabilities and user-friendly interfaces. The custom-developed mobile device seamlessly links the signal acquisition (from human motions to electrical signals), conditioning and processing (from analog to digital signals), wireless transmission and data interpretation (from digital signals to musical notes) in one platform. Such a wearable device allows one to produce music using smartphones through simple body motions in a more interactive and creative way. Moreover, this approach can also be applicable to fabricating other emerging wearable electronics for a variety of applications.

It is important for wearable sensors to be able to detect human motions in an accurate and reproducible manner. To verify the capabilities of sensing various body motions, the

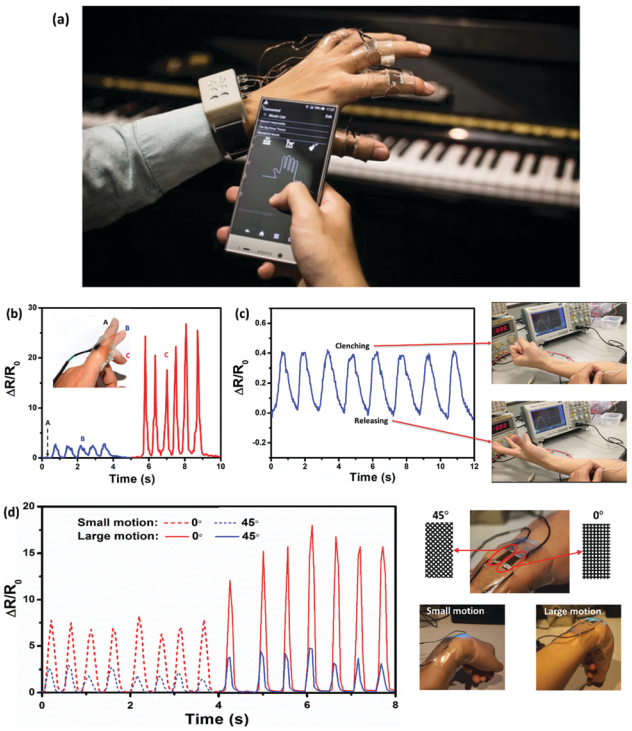

Fig. 4 (a) Schematic illustration of a wearable wireless musical instrument made from the GWF/PDMS sensors. Normalized resistance changes monitored during (b) finger bending and (c) cyclic clenching and releasing of forearm muscles. (d) Normalized resistance changes of two sensors with different GT orientations monitored during wrist bending.

GWF/PDMS composite sensors were attached to different body parts including the finger, upper arm, forearm and wrist, and the resistance changes due to different body motions were monitored simultaneously. The composite sensors were capable of sensing large joint motions of fingers. The bending of the fingers to different degrees led to uniquely different amplitudes of resistance changes (Fig. 4b). When mounted on the forearm, the composite sensors were able to capture the tiny muscle motions induced by clenching/releasing motions of the hand due to their extremely high sensitivities (Fig. 4c and Video 1, ESI†). The resistance changes during repeated clenching/releasing cycles remained very stable, demonstrating the accuracy and reproducibility of the composite sensor in detecting the same body motion. The sensors were also sensitive enough to record and discriminate tiny differences in muscle motions by virtue of the uniquely differentiated patterns of response curves when mounted on the upper arm and forearm, respectively (Fig. S10 and Video 2, ESI†). The unique orthotropic resistance changes of composite sensors were also exploited to generate different output signals with a single body motion. Besides fingers, the composite sensors were also capable of sensing joint motions of wrists. Two sensors with different GT orientations mounted onto the wrist generated two resistance changes with different amplitudes (Fig. 4d), signifying the capability to produce two distinct signals with one body motion. In summary, the GWF/PDMS composite sensors showed an excellent sensitivity to both small muscle and large joint

motions, high accuracy and reproducibility in response to the same body motion, an instantaneous response to various body motions and the unique capability of producing two signals with a single body motion.

The above features allow significant flexibility in accurate manipulations of different music notes by different body motions, and the possibility of playing chords with a single motion by exploiting the unique orthotropic nature of the sensor. As a proof of concept, a wearable piano was demonstrated by using several composite sensors mounted onto the fingers, which were capable of playing simple music such as *Ode to Joy* and *Jingle Bells* (Videos 4 and 5, ESI†). In analogy to a real piano, the bending of each finger corresponded to an individual note, and the finger motions triggered the playing of the notes instantaneously. A more advanced and unique feature of playing chords with a single body motion was also demonstrated by mounting two sensors with different GT orientations on the wrist (Video 3, ESI†). The single bending of the wrist produced a chord with different scales because the resistance changes in two sensors were different. Such a feature is unique to GWF/PDMS composite sensors and cannot be achieved using other types of sensors, which show an isotropic response to an external load.

The GWF/PDMS composite sensors were then integrated with hardware that had a Bluetooth wireless communication module and a custom developed smartphone application to form a wireless wearable music system, as illustrated in Fig. 5. The composite sensors were made wearable by embedding them in flexible H-shaped PDMS matrices (Fig. S9, see the ESI† for details), so that they could be wrapped around fingers or arms comfortably. To ensure the firm attachment of wearable sensors to various body parts, two pairs of buckles were installed at four ends of the H-shaped sensor. Compared to the commonly used medical tapes for fixing sensors,[65,66] these buckles ensured that the sensors were more easily put on and off, so that they could be used repeatedly. To realize simultaneous collection and transmission of motion signals, a werable hardware device consisting of an extension board, a control board and Li-ion button cells as the power supply were developed in-house. All the components were packed and protected in a 3D-printed plastic case (Fig. 5b) and could be worn using a wristband. The main function of the device was to process and transmit signals originating from the sensors to the remote smartphone *via* the Bluetooth 4.0 wireless communication. Fig. 5a shows the wired connections in the device and their distinct functions with different colors, *i.e.*, red lines for power supply (VCC, Voltage Collector-to-Collector), yellow lines for signal transmission and black lines for ground connection (GND, Ground). The extension board was designed to convert the resistance signals from the sensors to the voltage signals and transmit them to the control board for further processing. With six potentiometers placed in parallel (Fig. S11, ESI†), the extension board could accommodate up to six composite sensors working independently. Each composite sensor was connected to the designated potentiometer using sensor pins, while both the extension board and the control board were connected to the ground to ensure the same original reference

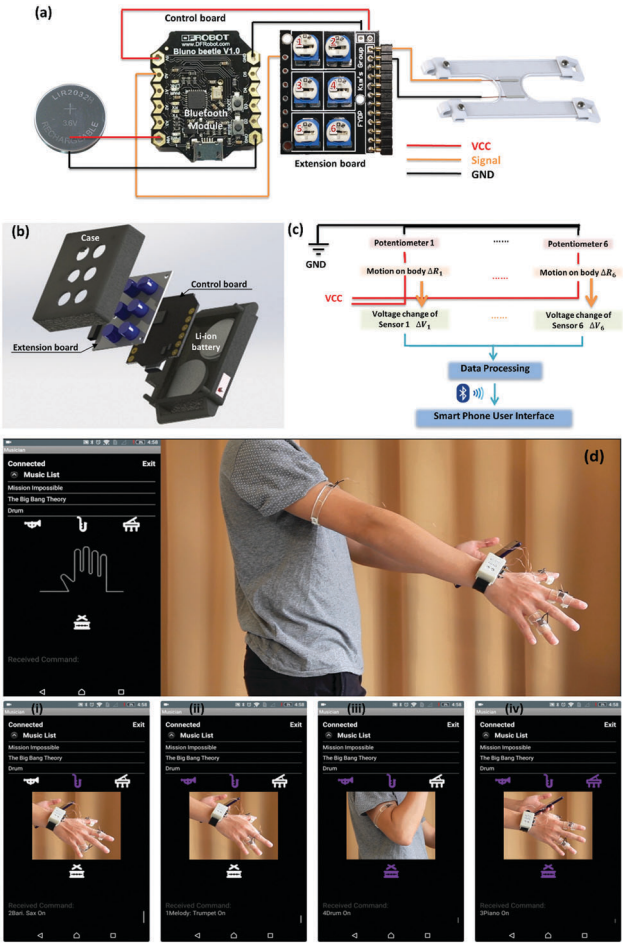

Fig. 5 (a) Circuit connection in the microcontroller device. (b) Layout of the wearable device and (c) block diagram of the wearable musical instrument, including signal transmission, processing and Bluetooth transmission to a smartphone. (d) User interface of Android apps on the smartphone; and (i–iv) real-time displays of relevant body motions.

electrical potentials for all potentiometers. The final analogue output (*i.e.* the voltage) of each sensor was tuned by the potentiometer to make sure the voltage was within the acceptable range. The coin-size control board (DFR0339-Bluno beetle V1.0) contained an analogue-to-digital converter and a Bluetooth 4.0 module, which guaranteed reliable data processing and high-speed communication between the sensors and the smartphone. A stable voltage was supplied by two rechargeable Li-ion batteries (LIR2032H) with a nominal voltage of 3.7 V and a capacity of 40 mA h. Fig. 5c shows the schematic flow chart of signal acquisition, processing and wireless data transmission in the wearable musical instrument. The motion signals were generated in the form of resistance changes in the GWF/PDMS composite sensors. The DC power and potentiometers converted the resistance signals to voltage signals, which were then transmitted through the analog input pins to the control board. The control board was programmed using the Arduino Integrated Development Environment (IDE) to read the output voltage from the extension board in the analog form and convert it to a digital form that could be interpreted by the

smartphone application. When the sensors were activated, the digital signals were transferred to the smartphone *via* Bluetooth 4.0 with a maximum transmission distance of 50 m. A mobile application (the Musician App) with user-friendly interface was designed in-house in the Android environment to read real-time data from the control board and allow the interaction between the user and the smartphone.

The final prototype of the wearable instrument in action is shown in Fig. 5d. Three sensors were attached to the fingers while one sensor was fixed around the upper arm, which monitored bending at finger joints and the motion of muscles on arm, respectively. When the Musician App started (Fig. 5d), the wireless connection between the control board and the smartphone was established and the sensors were automatically calibrated in a relaxed state, *i.e.* zero strain, by sending the original voltage information of each sensor to the smartphone *via* the control board. Users could choose different pre-recorded music files from the list, and each file consisted of multiple channels performed by different instruments. Each channel of musical files could be activated by triggering one of the four sensors with specific motions. Four icons of instruments representing respective channels will be highlighted when the corresponding channels are triggered (Fig. 5d(i–iv)). The users can rearrange melodies to play music by motions more interactively with their unique reinterpretation. In view of the potential application for health monitoring, we measured the relative resistance changes of the composite sensor attached on a wrist to monitor the pulse, as shown in Fig. S12 (ESI†). The composite sensor was sensitive enough to detect the very weak signals, and the pulse rate was determined to be 74 per min, confirming the capability of the sensor to detect tiny human physiological signals from skin-mountable application.

Conclusions

In summary, we present a GWF/PDMS composite that possesses a combination of extremely high GFs for strain sensing, high flexibility for wearable applications, and the capability to detect multi-mode deformations, such as tensile and flexural strains, for use as a wireless wearable musical instrument. The GWF consisting of highly conductive GTs interwoven in a well-defined interconnected mesh architecture served as an electrically conductive network in the composite to sense the applied strains to transmit output signals in the form of resistance change. By carefully controlling the quality of GWFs and the orientations of GTs, the flexible GWF/PDMS composites showed both a high sensitivity and high reversibility to tensile and bending loads as the piezoresistive sensors. Correlations were established between the applied strain and the resistance change in both 0° and 45° orientations, which were also proven by theoretical models.

The practical application of the composites as wearable devices was demonstrated by integrating them into a wearable musical instrument that is equipped with wearable interface and wireless communications. The semi-transparent and flexible GWF/PDMS composites served as wearable body motion sensors, which are able to translate human body motions to music *via* wireless Bluetooth communication and a smartphone. The unique architecture and versatile fabrication process can open new and promising potentials in wearable electronics, such as skin-mountable electronics for human health monitoring, wearable fitness tracking devices and communication systems for people with severe disabilities.

Author contributions

The manuscript was written through contributions of all authors. All authors have given approval to the final version of the manuscript. X. L., X. S., C. T., Q. B. Z. and J. K. K. conceived the idea. X. L. and Y. F. L. prepared the materials. X. L., Q. B. Z., and Z. Y. W. conducted the mechanical and electrical tests of materials. X. L. and Y. W. conducted the material characterization. X. L. and X. S. built the models and analyzed the data. X. H. D., C. T., S. Y. S., S. X. and Y. F. L. designed devices, packaged the hardware and wrote the programs for the smartphone App. A. H. provided suggestions in the computer music part. X. L. and X. S. wrote the manuscript instructed by Q. B. Z. and J. K. K. with input from all the authors.

Acknowledgements

This project was financially supported by the Research Grants Council of Hong Kong SAR (GRF Projects: 16203415 and 16229216). The project ''Graphene/PDMS Composites as Flexible Motion Sensors for Wearable Musical Instrument'' was awarded a 2016 HKUST President's Cup (Silver Award). The authors also appreciate the technical assistance from the Advanced Engineering Materials Facilities (AEMF) and the Materials Characterization and Preparation Facilities (MCPF) of HKUST.

References

1 M. Amjadi, K.-U. Kyung, I. Park and M. Sitti, *Adv. Funct. Mater.*, 2016, **26**, 1678–1698.
2 K. Kim, J. Kim, B. G. Hyun, S. Ji, S. Y. Kim, S. Kim, B. W. An and J. U. Park, *Nanoscale*, 2015, **7**, 14577–14594.
3 C. S. Boland, U. Khan, C. Backes, A. O'Neill, J. McCauley, S. Duane, R. Shanker, Y. Liu, I. Jurewicz, A. B. Dalton and J. N. Coleman, *ACS Nano*, 2014, **8**, 8819–8830.
4 N. Notman, *Mater. Today*, 2015, **18**, 358–359.
5 L. Winkless, *Mater. Today*, 2015, **18**, 63–64.
6 M. Amjadi, A. Pichitpajongkit, S. Lee, S. Ryu and I. Park, *ACS Nano*, 2014, **8**, 5154–5163.
7 B. U. Hwang, J. H. Lee, T. Q. Trung, E. Roh, D. I. Kim, S. W. Kim and N. E. Lee, *ACS Nano*, 2015, **9**, 8801–8810.
8 S. Gong, D. T. H. Lai, B. Su, K. J. Si, Z. Ma, L. W. Yap, P. Guo and W. Cheng, *Adv. Electron. Mater.*, 2015, **1**, 1400063.

9 T. Yang, X. Li, X. Jiang, S. Lin, J. Lao, J. Shi, Z. Zhen, Z. Li and H. Zhu, *Mater. Horiz.*, 2016, **3**, 248–255.
10 M. Segev-Bar and H. Haick, *ACS Nano*, 2013, **7**, 8366–8378.
11 J. Kim, M. Lee, H. J. Shim, R. Ghaffari, H. R. Cho, D. Son, Y. H. Jung, M. Soh, C. Choi, S. Jung, K. Chu, D. Jeon, S. T. Lee, J. H. Kim, S. H. Choi, T. Hyeon and D. H. Kim, *Nat. Commun.*, 2014, **5**, 5747.
12 N. Lu, C. Lu, S. Yang and J. Rogers, *Adv. Funct. Mater.*, 2012, **22**, 4044–4050.
13 T. Yamada, Y. Hayamizu, Y. Yamamoto, Y. Yomogida, A. Izadi-Najafabadi, D. N. Futaba and K. Hata, *Nat. Nanotechnol.*, 2011, **6**, 296–301.
14 J. Park, Y. Lee, J. Hong, Y. Lee, M. Ha, Y. Jung, H. Lim, S. Y. Kim and H. Ko, *ACS Nano*, 2014, **8**, 12020–12029.
15 S. Ryu, P. Lee, J. B. Chou, R. Xu, R. Zhao, A. J. Hart and S.-G. Kim, *ACS Nano*, 2015, **9**, 5929–5936.
16 Z. Liu, D. Qi, P. Guo, Y. Liu, B. Zhu, H. Yang, Y. Liu, B. Li, C. Zhang, J. Yu, B. Liedberg and X. Chen, *Adv. Mater.*, 2015, **27**, 6230–6237.
17 C. Sealy, *Mater. Today*, 2016, **19**, 7.
18 Y. Wang, R. Yang, Z. Shi, L. Zhang, D. Shi, E. Wang and G. Zhang, *ACS Nano*, 2011, **5**, 3645–3650.
19 M. Hempel, D. Nezich, J. Kong and M. Hofmann, *Nano Lett.*, 2012, **12**, 5714–5718.
20 C. Yan, J. Wang, W. Kang, M. Cui, X. Wang, C. Y. Foo, K. J. Chee and P. S. Lee, *Adv. Mater.*, 2014, **26**, 2022–2027.
21 J. Zhao, G. Wang, R. Yang, X. Lu, M. Cheng, C. He, G. Xie, J. Meng, D. Shi and G. Zhang, *ACS Nano*, 2015, **9**, 1622–1629.
22 Y. Cheng, R. Wang, J. Sun and L. Gao, *Adv. Mater.*, 2015, **27**, 7365–7371.
23 Y. Lin, S. Liu, S. Chen, Y. Wei, X. Dong and L. Liu, *J. Mater. Chem. C*, 2016, **4**, 6345–6352.
24 K. K. Kim, S. Hong, H. M. Cho, J. Lee, Y. D. Suh, J. Ham and S. H. Ko, *Nano Lett.*, 2015, **15**, 5240–5247.
25 X. Xiao, L. Yuan, J. Zhong, T. Ding, Y. Liu, Z. Cai, Y. Rong, H. Han, J. Zhou and Z. L. Wang, *Adv. Mater.*, 2011, **23**, 5440–5444.
26 M. Segev-Bar, A. Landman, M. Nir-Shapira, G. Shuster and H. Haick, *ACS Appl. Mater. Interfaces*, 2013, **5**, 5531–5541.
27 M. Zheng, W. Li, M. Xu, N. Xu, P. Chen, M. Han and B. Xie, *Nanoscale*, 2014, **6**, 3930–3933.
28 X. Li, T. Yang, Y. Yang, J. Zhu, L. Li, F. E. Alam, X. Li, K. Wang, H. Cheng, C.-T. Lin, Y. Fang and H. Zhu, *Adv. Funct. Mater.*, 2016, **26**, 1322–1329.
29 J. Zhao, C. He, R. Yang, Z. Shi, M. Cheng, W. Yang, G. Xie, D. Wang, D. Shi and G. Zhang, *Appl. Phys. Lett.*, 2012, **101**, 063112.
30 Q. Liu, J. Chen, Y. Li and G. Shi, *ACS Nano*, 2016, **10**, 7901–7906.
31 E. Roh, B. U. Hwang, D. Kim, B. Y. Kim and N. E. Lee, *ACS Nano*, 2015, **9**, 6252–6261.
32 Y. R. Jeong, H. Park, S. W. Jin, S. Y. Hong, S.-S. Lee and J. S. Ha, *Adv. Funct. Mater.*, 2015, **25**, 4228–4236.
33 D. J. Lipomi, M. Vosgueritchian, B. C. Tee, S. L. Hellstrom, J. A. Lee, C. H. Fox and Z. Bao, *Nat. Nanotechnol.*, 2011, **6**, 788–792.
34 C. Feng, Z. Yi, L. F. Dumée, C. J. Garvey, F. She, B. Lin, S. Lucas, J. Schütz, W. Gao, Z. Peng and L. Kong, *Carbon*, 2015, **93**, 878–886.
35 Y. Wang, L. Wang, T. Yang, X. Li, X. Zang, M. Zhu, K. Wang, D. Wu and H. Zhu, *Adv. Funct. Mater.*, 2014, **24**, 4666–4670.
36 T. Yang, W. Wang, H. Zhang, X. Li, J. Shi, Y. He, Q. Zheng, Z. Li and H. Zhu, *ACS Nano*, 2015, **9**, 10867–10875.
37 C. Wang, X. Li, E. Gao, M. Jian, K. Xia, Q. Wang, Z. Xu, T. Ren and Y. Zhang, *Adv. Mater.*, 2016, **28**, 6640–6648.
38 T. Q. Trung and N. E. Lee, *Adv. Mater.*, 2016, **28**, 4338–4372.
39 M. Huang, T. A. Pascal, H. Kim, W. A. Goddard and J. R. Greer, *Nano Lett.*, 2011, **11**, 1241–1246.
40 K. S. Kim, Y. Zhao, H. Jang, S. Y. Lee, J. M. Kim, K. S. Kim, J. H. Ahn, P. Kim, J. Y. Choi and B. H. Hong, *Nature*, 2009, **457**, 706–710.
41 V. M. Pereira and A. H. Castro Neto, *Phys. Rev. Lett.*, 2009, **103**, 046801.
42 S.-H. Bae, Y. Lee, B. K. Sharma, H.-J. Lee, J.-H. Kim and J.-H. Ahn, *Carbon*, 2013, **51**, 236–242.
43 Y. Lee, S. Bae, H. Jang, S. Jang, S. E. Zhu, S. H. Sim, Y. I. Song, B. H. Hong and J. H. Ahn, *Nano Lett.*, 2010, **10**, 490–493.
44 Y. A. Samad, Y. Li, S. M. Alhassan and K. Liao, *ACS Appl. Mater. Interfaces*, 2015, **7**, 9195–9202.
45 R. Xu, Y. Lu, C. Jiang, J. Chen, P. Mao, G. Gao, L. Zhang and S. Wu, *ACS Appl. Mater. Interfaces*, 2014, **6**, 13455–13460.
46 Y. Qin, Q. Peng, Y. Ding, Z. Lin, C. Wang, Y. Li, F. Xu, J. Li, Y. Yuan, X. He and Y. Li, *ACS Nano*, 2015, **9**, 8933–8941.
47 Y. A. Samad, Y. Li, A. Schiffer, S. M. Alhassan and K. Liao, *Small*, 2015, **11**, 2380–2385.
48 X. Li, P. Sun, L. Fan, M. Zhu, K. Wang, M. Zhong, J. Wei, D. Wu, Y. Cheng and H. Zhu, *Sci. Rep.*, 2012, **2**, 395.
49 X. Li, R. Zhang, W. Yu, K. Wang, J. Wei, D. Wu, A. Cao, Z. Li, Y. Cheng, Q. Zheng, R. S. Ruoff and H. Zhu, *Sci. Rep.*, 2012, **2**, 870.
50 T. Yang, Y. Wang, X. Li, Y. Zhang, X. Li, K. Wang, D. Wu, H. Jin, Z. Li and H. Zhu, *Nanoscale*, 2014, **6**, 13053–13059.
51 X. Lee, T. Yang, X. Li, R. Zhang, M. Zhu, H. Zhang, D. Xie, J. Wei, M. Zhong, K. Wang, D. Wu, Z. Li and H. Zhu, *Appl. Phys. Lett.*, 2013, **102**, 163117.
52 X. Liu, X. Sun, Z. Wang, X. Shen, Y. Wu and J. K. Kim, *ACS Appl. Mater. Interfaces*, 2015, **7**, 21455–21464.
53 J. Jia, X. Sun, X. Lin, X. Shen, Y. W. Mai and J. K. Kim, *ACS Nano*, 2014, **8**, 5774–5783.
54 X. Sun, X. Liu, X. Shen, Y. Wu, Z. Wang and J.-K. Kim, *Composites, Part A*, 2016, **85**, 199–206.
55 W. Wang, T. Yang, H. Zhu and Q. Zheng, *Appl. Phys. Lett.*, 2015, **106**, 171903.
56 P. Y. Huang, C. S. Ruiz-Vargas, A. M. van der Zande, W. S. Whitney, M. P. Levendorf, J. W. Kevek, S. Garg, J. S. Alden, C. J. Hustedt, Y. Zhu, J. Park, P. L. McEuen and D. A. Muller, *Nature*, 2011, **469**, 389–392.
57 X. Shen, X. Lin, N. Yousefi, J. Jia and J.-K. Kim, *Carbon*, 2014, **66**, 84–92.
58 H. Zhang, G. Lee, C. Gong, L. Colombo and K. Cho, *J. Phys. Chem. C*, 2014, **118**, 2338–2343.

59 S. Park, M. A. Shehzad, M. F. Khan, G. Nazir, J. Eom, H. Noh and Y. Seo, *Carbon*, 2017, **112**, 142–148.
60 X.-W. Fu, Z.-M. Liao, J.-X. Zhou, Y.-B. Zhou, H.-C. Wu, R. Zhang, G. Jing, J. Xu, X. Wu, W. Guo and D. Yu, *Appl. Phys. Lett.*, 2011, **99**, 213107.
61 H. Tian, Y. Shu, Y. L. Cui, W. T. Mi, Y. Yang, D. Xie and T. L. Ren, *Nanoscale*, 2014, **6**, 699–705.
62 X. Wang, Y. Qiu, W. Cao and P. Hu, *Chem. Mater.*, 2015, **27**, 6969–6975.
63 M. Xiao, T. Kong, W. Wang, Q. Song, D. Zhang, Q. Ma and G. Cheng, *Adv. Funct. Mater.*, 2015, **25**, 6165–6172.
64 Q. Liu, M. Zhang, L. Huang, Y. Li, J. Chen, C. Li and G. Shi, *ACS Nano*, 2015, **9**, 12320–12326.
65 Y. Khan, A. E. Ostfeld, C. M. Lochner, A. Pierre and A. C. Arias, *Adv. Mater.*, 2016, **28**, 4373–4395.
66 C. Pang, J. H. Koo, A. Nguyen, J. M. Caves, M. G. Kim, A. Chortos, K. Kim, P. J. Wang, J. B. Tok and Z. Bao, *Adv. Mater.*, 2015, **27**, 634–640.

